RSC Advances

PAPER

View Article Online
View Journal | View Issue



Cite this: *RSC Adv.*, 2014, **4**, 7528

# Single-crystalline and multiple-twinned gold nanoparticles: an atomistic perspective on structural and thermal stabilities

Rao Huang,[a] Yu-Hua Wen,*[a] Gui-Fang Shao,[b] Zi-Zhong Zhu[a] and Shi-Gang Sun[c]

Received 13th November 2013
Accepted 9th January 2014

DOI: 10.1039/c3ra46631k

www.rsc.org/advances

Morphologies of gold nanoparticles play an important role in determining their chemical and physical (catalytic, electronic, optical, *etc.*) properties. Therefore, a fundamental understanding of the morphological stability is of crucial importance to their applications. In this article, we employed atomistic simulations to systematically investigate the structural and thermal stabilities of gold particles with eight representative nanoshapes, including single-crystalline and multiple-twinned structures. Our investigation has revealed that the truncated octahedron and the octahedron possessed the best structural stability, while the tetrahedron and the icosahedron did the worst. Further analyses have discovered different thermal stabilities and diverse melting behaviors in these particles. Especially, an inhomogeneous melting of the icosahedron was disclosed, and the relevant mechanism was elucidated. This study provides significant insight not only into the experimental preparation of gold nanoparticles but also into the design of gold nanostructures with both high catalytic activity and excellent stability.

## 1. Introduction

Gold (Au), as one of the very first metals known, has fascinated people for five thousand years. Besides its widespread monetary and symbolic functions, gold has many practical applications in biomedicine, electronics, catalysis and other fields. In the past two decades, the rapid advances in nanotechnology have made it possible to construct matter with sufficient degree of control over the material size, shape, composition, and morphology.[1] At nanometer size, materials may exhibit exceptional physical and chemical properties not observed in their bulk counterpart. A confirmable fact is that gold has long been regarded as a poorly active catalyst, whereas Au nano-sized particles display surprisingly high catalytic activity for CO oxidation at a temperature as low as 200 K.[2] Beyond the potential applications for catalytic reactions,[3–5] Au nanoparticles have attracted persistently tremendous attention also for their remarkable properties, including intense surface plasmon resonances[6] and tailorable surface-enhancing spectroscopic effects.[7] These excellent performances have greatly extended their utility in fields such as drug delivery, biomedical imaging, heating, chemical and biological sensing, and catalysis.

As is well-known, the unique physical and chemical properties of metallic nanoparticles are determined not only by the portion of surface atoms but also by surface structures of the particles. The former is directly associated with the particle size, and the latter depends strongly on the particle shape. Especially, the catalytic reactions preferentially take place on surfaces, and the catalytic functionality of metallic nanoparticles is highly related to the structure of facets enclosing the particles. Therefore, the shape-controlled synthesis of metallic nanoparticles becomes a promising direction for precisely tuning their chemical activity, selectivity, and stability. After the pioneering work of El-Sayed and co-workers for the synthesis of cubic and tetrahedral platinum nanoparticles,[8] many efforts have been devoted to prepare metallic nanoparticles with different shapes such as cube, tetrahedron, octahedron, cuboctahedron, decahedron, and icosahedron, which are usually enclosed by low-index facets of {100} and {111}.[9–16] Recently, metallic nanoparticles with high-index facets have been successfully prepared by wet chemistry routes.[17,18] These nanoparticles exhibit much higher catalytic activity than those enclosed by low-index facets because of a large density of low-coordinated atoms situated on steps, ledges and kinks. These works have stimulated great interest in synthesis, characterization and chemical properties of high-index faceted nanoparticles.

As is aforementioned, the catalytic performance of nanoparticles depends highly on the surface structure of facets enclosing the particles. As a crystal grows, different planes grow with different rates. Crystal growth rates in the direction perpendicular to a high-index plane are usually much faster than those

[a]*Institute of Theoretical Physics and Astrophysics, Department of Physics, Xiamen University, Xiamen 361005, China. E-mail: yhwen@xmu.edu.cn; Fax: +86-592-218-9426; Tel: +86-592-218-2248*

[b]*Center for Cloud Computing and Big Data, Department of Automation, Xiamen University, Xiamen 361005, China*

[c]*State Key Laboratory of Physical Chemistry of Solid Surfaces, Department of Chemistry, Xiamen University, Xiamen 361005, China*

along the normal direction of a low-index plane. Hence, high-index planes are rapidly eliminated during particle formation and the final particle shape is dominated by the low-index planes. Resultantly, low-index facets with lower surface energies are absolutely predominant in the surface structures of the synthesized metallic nanoparticles, while very few of them are bound with high-index facets.[19] Recently, decahedral and icosahedral Au nanoparticles with five-fold (pentagonal) twinned structures have been successfully prepared by *N*,*N*-dimethylformamide (DMF).[20,21] Such multiple twinned nanoparticles may be stable because they adopted {111} terminated facets to minimize the total surface energy. These twinned nanoparticles are particularly interesting due to their unusual and crystallographically forbidden pentagonal symmetry and concomitant lattice strain.[22]

Although there are extensive studies on synthesis and characterization of polyhedral Au nanoparticles with different sizes and shapes, to the best of our knowledge, not much work has been performed for a thorough study of their surface structures and stabilities.[23,24] The importance of particle stability lies in two aspects. On one hand, the particle shape is determined by its surface structures and therefore is fundamentally linked to the important properties (especially reactivity and surface plasmon resonance) of Au nanoparticles. These Au nanoparticles will lose their unique properties once their shapes cannot be retained, or the surface structures are destroyed. Whether they can reserve their initial shapes and surface structures when they are subjected to heating or used in high temperature conditions is crucial for their industrial applications. On the other hand, there are different polymorphs adoptable for Au nanoparticles, as stated above, which morphology they will finally crystallize into is generally dependent upon the thermodynamic conditions during the growth process. Since the temperature is an important factor in the chemical equilibrium of synthesis, a fundamental understanding of the shape and thermal stabilities can facilitate the development of shape-controlled synthesis of Au nanoparticles.

In view that the previous studies on stabilities of Au nanoclusters generally focused on particles with specific shape under different sizes,[25] in this article, we present a systematic study of stability analysis of various Au nanoparticles bound with low-index facets by using atomistic simulations. Both single-crystalline and multiple-twinned nanoparticles were considered. The size-dependent structural stability of different shaped nanoparticles was first discussed. Subsequently, these nanoparticles were heated for the examination of their thermal and shape stabilities. An elaborate investigation was performed for both thermally driven shape evolution and melting behavior of the nanoparticles. This article is structured as follows: Section 2 briefly describes the simulation methods. Section 3 presents the calculated results, discussion and comparisons with available results. The main conclusions are summarized in the fourth section.

## 2. Simulation methodology

As mentioned above, Au nanoparticles, enclosed by low-index facets, have been more frequently observed compared with those by high-index facets in preparation. Therefore, we have first constructed five polyhedral shapes of single-crystalline Au nanoparticles, namely cube bound by six {100} facets, rhombic dodecahedron by twelve {110} ones, tetrahedron by four {111} ones, octahedron by eight {111} ones, and truncated octahedron by six {100} and eight {111} ones, from a large cubic face-centred cubic (fcc) single crystal, respectively. Particularly, the freezing of Au clusters into multiply twinned structures has been discovered.[26,27] Due to the importance of multiple-twinned Au particles at nanoscale science, decahedral and icosahedral Au nanoparticles with five-fold twinned structures, respectively enclosed by ten and twenty {111} facets, have also been investigated in this article. Note that the decahedron and the icosahedron can be formed by joining five and twenty tetrahedra, respectively. Additionally, spherical single-crystalline Au nanoparticles have also been constructed for comparison with the polyhedral ones. These Au nanoparticles of eight shapes have been illustrated schematically in Fig. 1. Similarly, a series of these Au nanoparticles with different sizes were modeled. Due to the limitation of present computer facilities available, the total number of atoms varies between 200 and 550 000.

Based on our previous works,[28–31] the quantum corrected Sutton–Chen (Q-SC) type potential has been adopted to describe the interatomic interactions of the nanoparticles. These potentials represent many-body interactions, and their parameters are optimized to describe the lattice parameter, cohesive energy, bulk modulus, elastic constants, phonon dispersion, vacancy formation energy, and surface energy, leading to an accurate description of many properties of metals and their alloys.[32,33] Generally good agreement was found with all properties of nine fcc metals (Al, Ni, Cu, Rh, Pd, Ag, Ir, Pt and Au).[34] The total potential energy for a system of atoms can be written as

$$U = \sum_i U_i = \sum_i \varepsilon \left[ \frac{1}{2} \sum_{j \neq i} V(R_{ij}) - c\sqrt{\rho_i} \right], \quad (1)$$

in which $V(R_{ij})$ is a pair interaction function defined by the following equation:

$$V(R_{ij}) = \left( \frac{a}{R_{ij}} \right)^n, \quad (2)$$

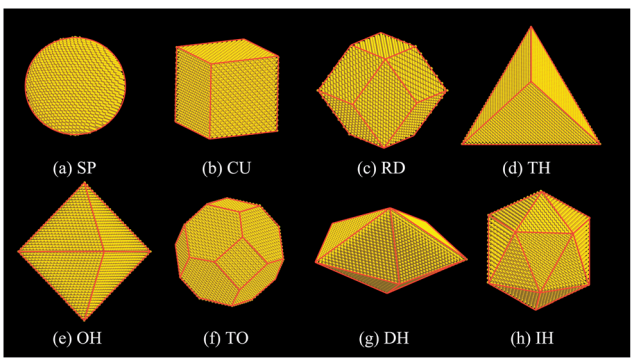


Fig. 1 Schematic illustration of eight shapes of Au single-crystalline particles (a) sphere (SP), (b) cube (CU), (c) rhombic dodecahedron (RD), (d) tetrahedron (TH), (e) octahedron (OH), (f) truncated octahedron (TO); and multiple-twined particles (g) decahedron (DH), (h) icosahedron (IH).

accounting for the repulsion between the $i$ and $j$ atomic cores; $\rho_i$ is a local electron density accounting for cohesion associated with atom $i$ defined by

$$\rho_i = \sum_{j \neq i} \left(\frac{a}{R_{ij}}\right)^m. \quad (3)$$

In eqn (1)–(3), $R_{ij}$ is the distance between atoms $i$ and $j$; $a$ is a length parameter scaling all spacings (leading to dimensionless $V$ and $\rho$); $c$ is a dimensionless parameter scaling the attractive terms; $\varepsilon$ sets the overall energy scale; $n$ and $m$ are integer parameters such that $n > m$. Given the exponents ($n$, $m$), $c$ is determined by the equilibrium lattice parameter, and $\varepsilon$ is determined by the total cohesive energy. The model parameters for Au are given as follows: $n = 11$, $m = 8$, $\varepsilon = 7.8052$ meV, $c = 53.581$, and $a = 4.0651$ Å.[34]

Upon starting the molecular dynamics (MD) simulations, the total energy minimization process of all Au nanoparticles has been first preformed through the conjugate gradient methods.[35] The total energy could be obtained by summing the potential energy of each atom in the nanoparticles. After full relaxation, all the eight types of nanoparticles with size of about 6 nm were subjected to a continuous heating. To make the simulations more reliable, we employed constant volume and temperature molecular dynamics (NVT-MD) to allow energy fluctuations, which may be critical to the resulting dynamics. The nanoparticles have undergone the heating process consisting of a series of NVT-MD simulations from 0 to 1500 K with a temperature increment of 50 K. However, a smaller step of 10 K has been adopted to investigate the melting behavior more accurately when the temperature went up to around the melting point. The simulations were carried out for 200 ps of the relaxation time at each temperature. Meanwhile, the statistical quantities were obtained in the last 25 ps. The desired temperature and ambient pressure were maintained by Nose–Hoover thermostat[36] and Berendsen approach,[37] respectively. The equations of atomic motion were integrated by the Verlet-Velocity algorithm[38] with a time step of 1.0 fs.

## 3. Results and discussion

### 3.1 Structural stability

The energetic stability of different structures for materials can be determined by the total energy which is equal to the summation of the potential energy of each atom at ground state since the kinetic energies are actually zero at absolute zero. The criterion indicates that the structure with lower energy tends to be more stable. In order to facilitate the comparison of Au nanoparticles with different shapes, a common definition of particle size, based on equivalent volume, has been introduced as follows:

$$d = \sqrt[3]{\frac{N}{4}} a_0, \quad (4)$$

where $N$ is the total number of atoms in the particle, and $a_0 = 4.0651$ Å is the lattice constant of bulk Au. Since there are four atoms in each unit cell for fcc metals, the volume of each atom could be regarded as $a_0^3/4$. Note that not all of the eight shapes can be well formed when the particle size is less than 1 nm.

Fig. 2 presents the size dependent energy for the fully relaxed Au nanoparticles at ground state, where the particle size is from 1 to 22 nm. In this figure, the lower-energy particles possess better structural stability. In order to extrapolate the size effects on structural stability to larger particles, we proposed an analytic expression of the total energy according to particle constitution: considered that a polyhedral particle consists of atoms located in its interior, facets, edges, and vertices, the average energy per atom in the particle can be formulated as

$$\overline{E} = \frac{1}{N}\left(N_i\overline{E}_i + N_f\overline{E}_f + N_e\overline{E}_e + N_v\overline{E}_v\right) = A + \frac{B}{d} + \frac{C}{d^2} + \frac{D}{d^3} \quad (5)$$

where $N$, $N_i$, $N_f$, $N_e$, and $N_v$ is the atomic number of the system, interior, facets, edges, and vertices, respectively; $\bar{E}$, $\bar{E}_i$, $\bar{E}_f$, $\bar{E}_e$, and $\bar{E}_v$ is the average energy per atom of the system, interior, facets, edges, and vertices, respectively. The polynomial function above was hence adopted to fit the data of atomistic simulations with the framework of the least square method. The fitted curves are also depicted in Fig. 2, showing the excellent accordance with the simulated data. Also, these curves were further extrapolated to 100 nm to examine the stability of larger particles, as demonstrated in the inset figure.

As seen in Fig. 2, all the particle energies are significantly decreased with rising size, indicating a strong size effect. In addition, the energy differences between shapes illustrate a prominent surface effect in these nanoparticles. This phenomenon has already been observed in the previous studies on nanoscale materials.[28,33] Fig. 2 also reveals that for $d < 10$ nm, the tetrahedron exhibits the worst stability. However, beyond 10 nm, the least stable shape is icosahedron, which has remarkably higher energy than the other seven shapes. Meanwhile, the instability of the cube respectively ranks the second and the third among all the shapes demarcated by 7.8 nm or so. Interestingly, the sphere is not the most stable shape although its surface area is theoretically the smallest in all particles of the same size. Instead, the truncated octahedron and octahedron invariably display the best and the second best stability, respectively. The sphere is the third most stable shape when $d$ falls into the range from 3.2 to 57 nm. Otherwise, the third place

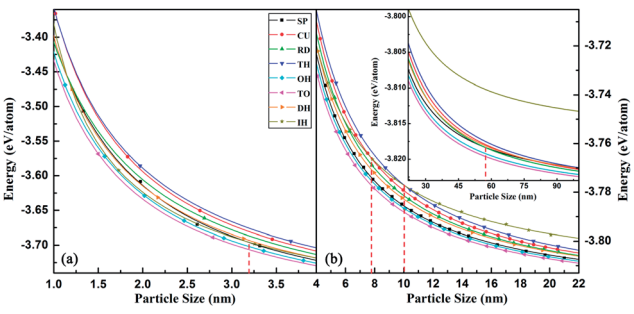


Fig. 2 Size-dependent ground-state energies of eight types of Au particles with size from (a) 1.0 to 4.0 nm and (b) 4.0 to 22 nm. Inserted picture: the results of Au particles with large size between 22 and 100 nm predicted from the fitted curves.

is replaced by the icosahedron for the particle size smaller than 3.2 nm or by the rhombic dodecahedron for the particle size above 57 nm. Besides, by comparing the total energy of the two twinned nanoparticles, the icosahedron is more stable than the decahedron for the particle size below 4 nm.

On account of a high surface-to-volume ratio, the surface contribution to the total energy of a nanoparticle becomes pronounced, and the surface effects will play dominant roles in determining the structural stability of the nanoparticle since there is no discernible difference in the energies of interior atoms for single-crystalline particles. As is known, the surface energy of low-index planes that determine the shapes of these nanoparticles is generally increased in the order of $\gamma_{\{111\}} < \gamma_{\{100\}} < \gamma_{\{110\}}$.[39–41] Therefore, it is not surprising to find that the octahedron, enclosed by {111} facets, and the truncated octahedron, enclosed by eight {111} facets and six {100} facets, are both more stable than the cube and the rhombic dodecahedron which are respectively terminated by {100} and {110} facets. Nevertheless, the surface energy is not the only deciding factor in the evaluation of structural stability since the surface-to-volume ratio also has a contribution to determining the structural stability. This is why the tetrahedron is more unstable than the octahedron and even the cube and rhombic dodecahedron, although it is enclosed by {111} planes. Similarly, this can be used to explain why the cube and octahedron has a worse stability compared with the rhombic dodecahedron and the truncated octahedron, respectively. The same tendency has also been observed in our previous study on Pt nanoparticles.[28] Essentially, the fundamental reason should be associated with the relative ratios of surface energies of the three low-index crystallographic planes.[42]

For the five-fold twinned structures, namely the decahedral and the icosahedral particles, the case is more complicated than that in the single-crystalline particles due to the existence of twin boundaries. As is described in Section 2, the decahedral nanoparticle consists of five juxtaposed tetrahedral crystallites bound by {111} facets (see Fig. 1g). Theoretically, the angle between two adjacent {111} planes is 70.53°. Hence, a gap of 7.35° is generated when joining five tetrahedra.[43] In this case, the space cannot be filled simply by joining five tetrahedra and some form of internal strain is hence required to close the gap.[42] Similarly, the icosahedron is formed by the junction of twenty tetrahedra with twinning on their {111} planes (see Fig. 1h), and the internal strain is necessary because of the multiple twinned nature of the structure.[42] Therefore, the existence of twin boundaries will introduce the extra energy into the twinned particle compared with the single-crystalline structures, providing a significant contribution to the total energy. It explains why the twinned particles exhibit worse stability than most of the single-crystalline ones, especially as the size of the particle increases. Exceptionally, the decahedral twinned particles exhibit better stability than the tetrahedral single-crystalline ones for the particle size within 100 nm although they are both enclosed by {111} facets. This is mainly originated from higher surface energy induced by the relatively large surface area of the tetrahedron. For example, the surface-to-volume ratio is 0.1105, 0.0953, and 0.0736 $Å^{-1}$ at the particle size of 6 nm for the tetrahedron, decahedron and icosahedron, respectively. It also indicates that in the twinned particles, the excessive energy, associated with the internal strain and stacking faults, can be compensated partly by reducing their surface area. However, as the particle further grows, the surface energy decreased by pure exposure of {111} facets is not capable of exceeding the extra energy required to retain the multiple-twinned structures and the particle will progress into single-crystalline structures.[42] Accordingly, the twinned particles are favored at small sizes and single-crystalline ones are preferred at large sizes, which has been experimentally verified by transmission electron microscopy characterization for synthesized fcc Fe nanoparticles.[44,45]

### 3.2 Thermal stability

Understanding of thermal stability of Au nanoparticles is particularly acute for both their chemical synthesis and ultimate application. Due to the low Tammann temperature of Au (395 °C), Au nanoparticles are easily sintered under heating, which limits their operating temperatures.[46] When they are used for catalytic reactions at elevated temperatures,[47] the nanoparticles tend to aggregate into large particles, thus requiring reasonable control of the synthesis temperature to prevent their sintering and coarsening. Therefore, the investigation of the thermal stability of Au nanoparticles is of technological importance for their industrial applications. In this article, MD simulations of a continuous heating process were performed on the eight types of Au nanoparticles with around 13 000 atoms (corresponding to a particle size of 6 nm) to examine their thermal stabilities.

MD simulations can provide elaborate information concerning the thermodynamic properties, the characteristics and progress of melting during heating process. The phase transition temperature from solid to liquid is usually identified by monitoring the variation in the thermodynamic quantities such as potential energy and heat capacity. The melting point is defined as a temperature at which the heat capacity reaches its maximum. The potential energy can be obtained from MD simulations of the heating process and the specific heat capacity can hence be induced from the following equation

$$C_p(T) = \frac{dU}{dT} + \frac{3}{2}R_{gc}, \quad (6)$$

where $U$ is potential energy, and $R_{gc} = 8.314$ J mol$^{-1}$ K.

Fig. 3 illustrates the temperature dependence of potential energy as well as specific heat capacity for the eight types of Au nanoparticles. Note that the horizontal axis is broken at 900 K to highlight the phase transition region. Evidently, the potential energy exhibits a steady and linear increase below 900 K, leading to a constant heat capacity. Afterwards, sharp rises of the potential energy and accordingly abrupt peaks of the heat capacity emerge in the range from 1050 to 1100 K, indicating the occurrence of solid to liquid phase transition. As the nanoparticles completely melted into liquid, the potential energy would resume the linear dependence of temperature (not displayed here). The melting temperature $T_m$ is 1070, 1060,

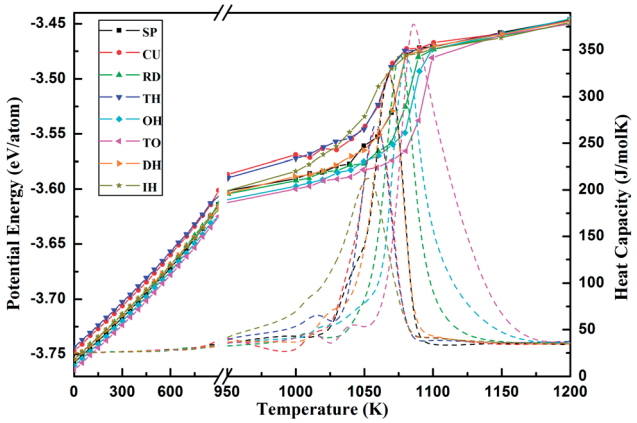


Fig. 3 Temperature-dependent potential energies (solid lines) and specific heat capacities (dashed lines) of eight Au nanoparticles with different shapes during the continuous heating.

1080, 1060, 1090, 1090, 1070, and 1060 K for the sphere, cube, rhombic dodecahedron, tetrahedron, octahedron, truncated octahedron, decahedron, and icosahedron, respectively. These temperatures are all remarkably lower than the melting point of bulk Au (1338 K for experimental value and 1380 K for theoretical calculations).[48] This reduction should be attributed to the high surface-volume ratio in nano-sized particles and low surface premelting temperature associated with the weak bonds among the low-coordinated surface atoms, which have been verified in the previous research.[28,32,49] Moreover, it can be seen from the melting points that the octahedron and truncated octahedron exhibit the best thermal stability, while the cube, tetrahedron and icosahedron the worst. Analogous to the structural stability, the thermal stability also seems to rely on various factors. The highest $T_m$ of the octahedron and truncated octahedron can be attributed to the lowest-energy {111} surfaces. Meanwhile, the worst thermal stability may stems from the large surface-to-volume ratio for the tetrahedron and low-coordinated surface atoms on {100} facets for the cube. As for the decahedron and icosahedron, their stabilities should be related to the existence of numerous twin boundary atoms that introduce relatively high interfacial energy.

Despite the determination of melting points, a natural anticipation is to further explore the nature of thermal stabilities of these nanoparticles and to elucidate the stability-associated phenomena. Generally, the melting mechanism can be clarified by analysis of the structural changes, diffusion coefficients, root-mean-squared displacement of atoms and so on. Among all the methods currently available, the Lindemann index, as a simple but effective measurement, is frequently used to characterize the thermal evolution of a system. It provides a good description of the thermally driven disorder. For a system of $N$ atoms, the local Lindemann index for the $i$th atom is defined as the root-mean-squared (RMS) bond length fluctuation as[50]

$$\delta_i = \frac{1}{N-1}\sum_{j\neq i}\frac{\sqrt{\langle R_{ij}^2\rangle - \langle R_{ij}^2\rangle}}{\langle R_{ij}\rangle}, \quad (7)$$

and the system-averaged Lindemann index is calculated by

$$\delta = \frac{1}{N}\sum_i \delta_i, \quad (8)$$

where $R_{ij}$ is the distance between the $i$th and $j$th atoms. The Lindemann index was originally developed to study the melting behavior of bulk crystals.

The Lindemann criterion suggests that the melting occurs when the index is in the range of 0.1–0.15, depending on materials,[51] while a small critical index of about 0.03 was normally adopted in clusters and homopolymers due to the relaxed constraint of the surface atoms.[50] The temperature dependent Lindemann indices during the heating process for the eight types of Au nanoparticles are illustrated in Fig. 4.

In accord with the potential energy curves in Fig. 3, the Lindemann indices basically exhibit a similar variation. In the initial stage, they increase slowly and linearly with rising temperature. At around 1000 K, they begin to deviate from the linear increase and show sharp jumps around the melting points, precisely corresponding to the abrupt rise of potential energy. Subsequently, the Lindemann indices continue to increase linearly (not presented here). Generally, the critical value of the Lindemann index is dependent on the constituent elements and their structures. In this work, it could be appropriately ascertained to be 0.038 for Au nanoparticles, as indicated by the dashed line in Fig. 4.

In order to visualize the melting process and to shed light on the melting mechanism, we have examined microscopic structural evolution of Au nanoparticles during continuous heating. Analogous to the study of melting of a surface-free Lennard-Jones crystal,[52] the concept of the Lindemann atom has been introduced into the current work. In the Lindemann melting criterion, an atom whose Lindemann index is larger than the critical value is defined as a Lindemann atom. The atomistic snapshots of these nanoparticles taken at representative temperatures have been extracted from the data records of the

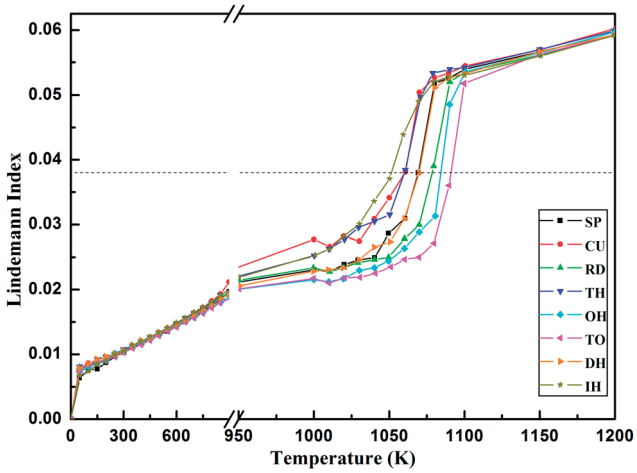


Fig. 4 Temperature-dependent Lindemann index for eight Au nanoparticles during the heating process. Dashed line indicates the critical Lindemann index of 0.038.

MD simulations, as depicted in Fig. 5 for single-crystalline particles and Fig. 6 for five-fold twinned ones.

Fig. 5 displays the thermal evolution of single-crystalline cube, rhombic dodecahedron, tetrahedron, octahedron, and truncated octahedron from polyhedral to sphere-like morphology prior to the overall melting. Note that the sphere is not demonstrated here because of its commonly homogeneous melting mode from surface into core.[53] It can be observed from Fig. 5 that all the nanoparticles were capable of maintaining their initial shapes and ordered surface structures at room temperature of 300 K. With the rising temperature, different thermal evolutions appeared among the polymorphs, although the melting proceeded gradually from the surface into the interior. For the cube, atoms located at the vertices have moved firstly at 600 K. They migrated inward and pushed against their coordinated atoms, resulting in the formation of {111} facets, as marked by the blue triangle (see Fig. 5a). The emergence of {111} facets is beneficial to minimizing the surface energy of the nanoparticle to a certain extent. At this temperature, only a few atoms at the edges have turned into Lindemann atoms. As the temperature was further elevated to 900 K, the number of Lindemann atoms distinctly increased, and they were basically distributed at the vertices and the edges. In contrast, most of the atoms on {100} facets retained their fcc arrangements. Additionally, the {111} facets at the vertices were enlarged to some extent, forming a truncated-cube-like particle. Hereafter, at 1050 K, the cube has transformed into a sphere-like shape and the initial surface structures have been completely destroyed. Similarly, the premelting in the other four polyhedral Au nanoparticles was preferentially nucleated at the active sites of the vertices. With the progress of melting, the vertices gradually disappeared and the edges became obtuse and undistinguishable, finally leading to an overall surface melting. As we know, the binding energy of an atom is mainly contributed by its first nearest-neighbors and is much less relevant with their second nearest-neighbors, while other atoms almost make no contribution. Consequently, the low-coordinated atoms are less confined and movable. For example, the numbers of the first and second nearest-neighbors of vertex atoms are 3 and 0 for tetrahedron, while 4 and 1 for octahedron. Therefore, the vertices in the tetrahedron are less stable than those in the octahedron although the two polyhedra are both bound by {111} facets, which can be verified by comparing their snapshots at 1000 K (Fig. 5c and d). On the other hand, the better thermal stability of {111} facets than {100} ones is clearly demonstrated by the snapshot of truncated octahedron at 1080 K, in which the majority of Lindemann atoms have concentrated on the {100} facets while only a small portion of them are distributed on the {111} facets (see Fig. 5e). This phenomenon is in accordance with the conclusions of previous studies: at a temperature close to the particle melting point, most of the solid-like surface atoms are found belonging to {111} planes.[54] The better stability of {111} facets can be attributed to the fact that surface atoms are eight-coordinated for {100} planes while nine-coordinated for {111} ones. Therefore, it is comprehensible that in single-crystalline structures, the best thermal stability occurs at the purely {111} faceted octahedron and the truncated octahedron

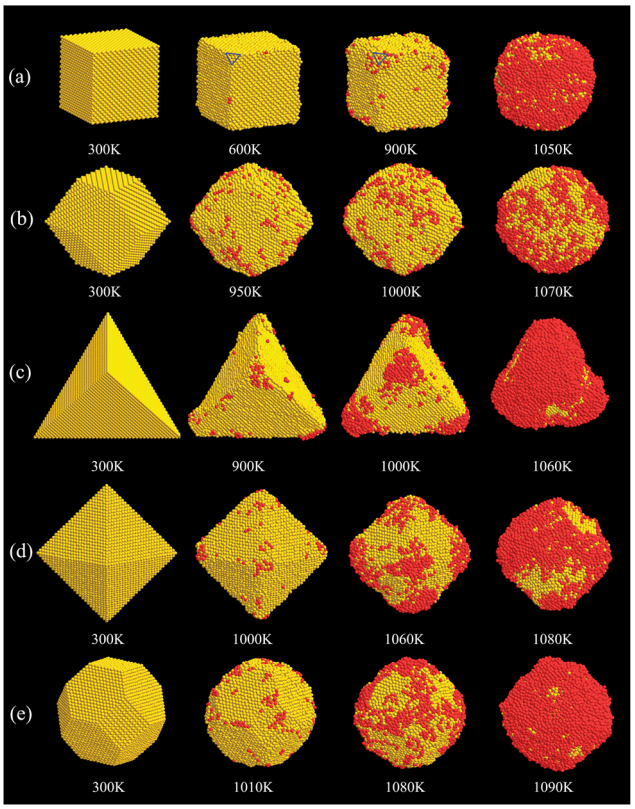


Fig. 5 Snapshots of the single-crystalline Au nanoparticles taken at four representative temperatures during the heating process, respectively. (a) cube, (b) rhombic dodecahedron, (c) tetrahedron, (d) octahedron, and (e) truncated octahedron. Coloring denotes type of atom: gold, Au non-Lindemann atom; red, Au Lindemann atom.

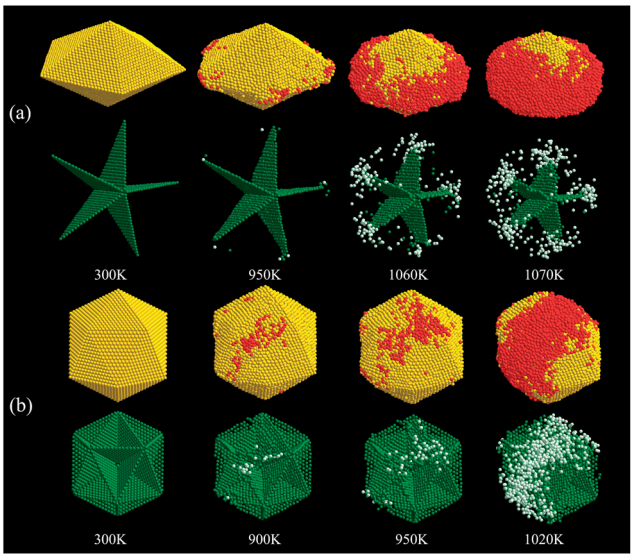


Fig. 6 Snapshots of the five-fold twinned Au nanoparticles and their twin boundaries taken at four representative temperatures during the heating process, respectively. (a) Decahedron, and (b) Icosahedron. Coloring denotes type of atom: gold, Au non-Lindemann atom; red, Au Lindemann atom; green, non-Lindemann boundary atom; light green, Lindemann boundary atom.

in which vertex atoms are also highly coordinated (the number of their first and second nearest-neighbors is 6 and 2, respectively). In contrast, the tetrahedron and the cube consequently possess the worst thermal stability. As for the rhombic dodecahedron, although it is enclosed by the most unstable {110} facets among the three low-index facets, its medium thermal stability may be originated from the moderate coordination of vertex atoms: the number of their first nearest-neighbors can take values of 3, 4 or 7, depending on the vertex position.

Fig. 6 presents the representative snapshots of five-fold twinned decahedron and icosahedron during the heating process. To perform a detailed analysis, the movements of those atoms initially situated at twin boundaries were particularly traced. Probably due to the relatively small size of the two nanoparticles, no stacking fault was observed in characterization of the local crystal structures by the common neighbor analysis (CNA).[55] As illustrated in Fig. 6a, the melting progress in the decahedron is generally similar to what happened in the single-crystalline nanoparticles: the disorder was gradually expanded from the five vertices to the five horizontal adjacent edges then to the entire surface, finally leading to the overall melting of the particle. The better stability of the top and bottom apexes is aroused from their higher coordination number compared with that of the remaining five vertex atoms: the number of the first and second nearest-neighbors is 6 and 0 for the former, respectively; while 4 and 0 for the latter, respectively. By comparison, the icosahedron distinctly exhibited a typical inhomogeneous melting different from the decahedron (see Fig. 6b). At 900 K, a few Lindemann atoms have emerged on the surfaces and primarily concentrated on one of twenty facets. Meanwhile, the twin boundaries near this facet have accordingly been destroyed to some extent, where some of atoms have even melted. However, the ordered structure was roughly maintained in other region, displaying an inhomogeneous characteristic. Afterwards, the melting has penetrated from the facet into the interior with increased temperature, and further extended to the neighboring tetrahedron. It can be deduced that this inhomogeneity comes from the existence of twin boundaries. As is known, the thermal vibrations of atoms in the particle would be intensified with rising temperature, and the solid–liquid phase transition is determined by their diffusive behaviors. Nevertheless, the diffusion of these thermally vibrated atoms in each tetrahedron was hindered by the twin boundaries. Those atoms located at twin boundaries possess high driving forces due to the lattice mismatch and internal strain. With the temperature increasing to a sufficiently high value, they will be easily diffusive and become disorder, resulting in the destruction and the premelting of twin boundaries. Meanwhile, since the simultaneous thermal activation of the premelting in all the twenty tetrahedra requires relatively high input of energy, therefore the melting preferentially started in one or two of these tetrahedra. It should also be noticed that owing to the different geometry in the decahedron and the icosahedron, the twin boundaries in the former were not able to effectively hinder the movements of atoms at five apices since they may easily diffuse to the region outside the twin boundaries. Consequently, the disorder at the apices will not necessarily induce a large area destruction of twin boundary. As a result, the similar inhomogeneous melting was not observed in the decahedron, as seen in Fig. 6a. Besides, some studies has found that facets on the surface of icosahedral Au nanoparticles 'softened' but remained ordered and did not premelt below the particle melting temperature.[25] In their analysis, the authors quantified their findings by computing the curvature distribution of the surface using the average position of the surface in a given solid angle and its nearest neighbors. By defining the normal to this plane as the *z*-axis, they determined the paraboloid-of-best-fit to approximate the two principal curvatures of the surface at the given solid angle. However, we believe that surface premelting (including homogeneous[53] and nonhomogeneous[25]) or structural disordering prior to the melting of the whole nanoparticle happens more frequently in most observations.

### 3.3 Shape evolution

As is known, surface structures of nanoparticles are crucial for their chemical and physical properties. However, it is rather difficult to precisely determine whether and when the surface structures of particles become destroyed under heating process. Note that the particle shape is highly dependent on its surface structures (*i.e.* the Miller index of surface). Therefore, the shape change is a mirror of surface transformation. Based on this consideration, we have quantitatively obtained information concerning the shape evolution of the eight particles during the continuous heating by introducing a shape factor $S$ as follows:[56]

$$S = \frac{1}{R^2}\sqrt{\frac{1}{N}\sum_{i=1}^{N}\left(r_i^2 - R^2\right)^2}, \tag{9}$$

in which $r_i$ is the distance of atom $i$ from the particle center of mass and $R$ is the RMS of $r_i$:

$$R = \sqrt{\frac{1}{N}\sum_{i=1}^{N} r_i^2}. \tag{10}$$

According to this definition, $S$ is independent on atomic number $N$ and is only associated with particle shape for all the fcc structures. Fig. 7 illustrates the calculated results for all the eight types of Au nanoparticles. Evidently, different particle morphologies possess different values of $S$, although there is no distinct discrepancy between those of certain shapes (for examples, cube and octahedron, truncated octahedron and icosahedron). At the low temperature region, each particle can maintain its initial shape. In this region, no observable change of the surfaces could be identified from the corresponding snapshots. With further increased temperature, all the shape factors, except for that of the sphere, drop down to different extents and are finally close to 0.44, which is slightly higher than the initial shape factor of the sphere. The deviation of the shape factors from their initial values is mainly attributed to the diffusive behavior of atoms.

According to Fig. 7, the startup temperature of the deviation is ascertained to be 800, 850, 800, 950, 1150, 850, 950 K for the

 

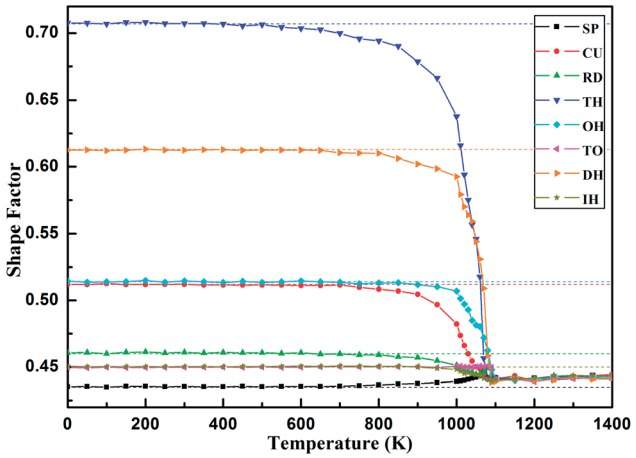


Fig. 7 Shape factors of the eight Au nanoparticles at different temperatures. Dashed lines indicate the corresponding initial values.

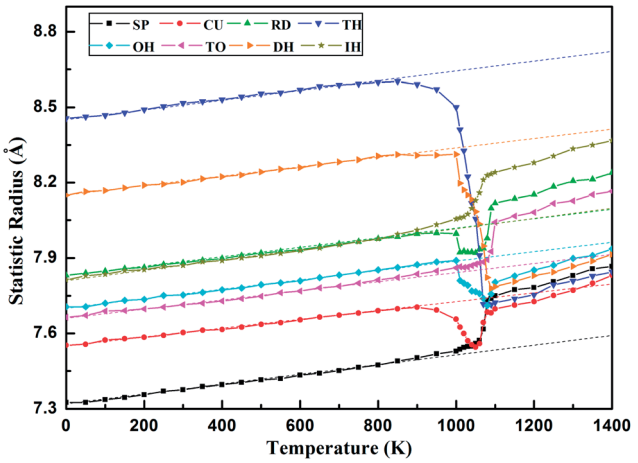


Fig. 8 Temperature dependence of normalized statistical radii of the eight Au nanoparticles during the heating process. Dashed lines indicate the corresponding linear extrapolation values.

cube, rhombic dodecahedron, tetrahedron, octahedron, truncated octahedron, decahedron and icosahedron, respectively. These starting temperatures, at which a noticeable migration of surface atoms occurs, are partly consistent with the melting points of the particles: the tetrahedron with the lowest $T_m$ also firstly initiated its shape transformation, and the most stable truncated octahedron did lastly. Nevertheless, the icosahedron which exhibited the least thermal stability retained its shape until a relative high temperature. This may be associated with its approximately spherical shape compared with the other six polyhedra. Similarly, the octahedron changed earlier than the truncated octahedron because of its "sharper" shape, though the $T_m$ is almost equal for the two particles. Moreover, the shape factors of different structures converge to the same value at high temperatures, indicating all the particles finally evolved into the same shape after overall melting.

As is aforementioned, there is no correlation between the shape factor and the atomic number of particle. However, the statistical radius, related to the atomic number and the particle size, can also provide indication of surface destruction and shape change from the other hand. The concept of statistical radius is adopted by the following equation[32]

$$R_N = \sqrt{\frac{5}{3}\frac{1}{N}\sum_{j=1}^{N}(R_j - R_{cm})^2}, \quad (11)$$

where $(R_j - R_{cm})$ is the distance of atom $j$ from the particle center of mass. Due to the fact that the number of atoms in each nanoparticle is different, the statistical radius was normalized with respect to the atomic number $N$ by the equation[57]

$$R = R_N/N^{1/3}, \quad (12)$$

As is shown in Fig. 8, for an fcc system, the statistical radii are larger for the particles of polyhedral shapes than that of the spherical one with the same atomic number. All the statistical radii are linearly increased when the temperature is below 700 K. This result is definitely originated from the lattice thermal expansion in the particles, indicating no noticeable change in both shape and surface structures. The average linear coefficient of thermal expansion, derived from the data in Fig. 8, is about $2.4 \times 10^{-5}$ K$^{-1}$, significantly higher than that of bulk Au ($1.4 \times 10^{-5}$ K$^{-1}$).[58] The enhanced thermal expansion coefficient of Au nanoparticles has also been verified experimentally.[59] Furthermore, as the heating proceeded, the deviation of $R$ from the initial linear increase occurred: the statistic radii of the cube, rhombic dodecahedron, tetrahedron, octahedron, and decahedron were continuously decreased in different degrees and reached their minimum, which can be consistently explained by the shape transformation induced by surface melting. However, the spherical nanoparticle exhibits a behavior different from the five nanoparticles above. The radius of spherical particle continually increases with rising temperature, and no shape change can be found before it melts entirely. For the truncated octahedron and icosahedron, the sphere-like shape makes them exhibit the similar behavior as the sphere. Finally, after the overall melting, all the statistic radii resume their linear increases, suggesting invariable shapes.

## 4. Conclusions

In this article, morphology and stability of Au NPs with both single-crystalline and multiple-twinned structures have been systematically examined by atomic simulations. Structural stability of Au particles with sizes below 100 nm was firstly investigated for eight diverse shapes. Subsequently, different thermal stabilities were identified for these particles, and the measurements of Lindemann index, shape factor, and statistic radius were employed to shed light on their melting behaviors and shape evolutions during continuous heating. The major conclusions are summarized as follows:

(1) The truncated octahedron and octahedron display best structural stability among all the shapes. By contrast, the most unstable shape is the tetrahedron for the particle size below 10 nm and the icosahedron for the particle size above 10 nm.

(2) The tetrahedron possesses the worst thermal and shape stabilities, while the truncated octahedron does the best.

(3) An inhomogenous melting behavior in the icosahedron is disclosed, which should be attributed to the existence of twin boundaries hindering the atomic diffusion.

(4) The coordination number is a decisive factor in determining where the premelting initiates: those low-coordinated atoms at apices are generally easier to be thermally activated in heating process.

These results, as mentioned above, suggest that the stability property of Au nanoparticles could be tunable by adjusting their shapes. The implications of these conclusions are not just limited to the Au system and can be broadened to other fcc metallic nanoparticles. The current study not only provides theoretical basis for the synthesis and application of polyhedral metallic nanoparticles but also is expected to motivate the further design of metallic nanostructures with both excellent performance and outstanding stability.

## Acknowledgements

This work is supported by the National Natural Science Foundation of China (grant nos 51271156 and 11204252), the Natural Science Foundation of Fujian Province of China (grant no. 2013J06002), and the Fundamental Research Funds for the Central Universities of China (grant no. 2012121010).

## Notes and references

1 P. K. Jain, I. H. El-Sayed and M. A. El-Sayed, *Nano Today*, 2007, **2**, 18–29.
2 M. Haruta and M. Date, *Appl. Catal., A*, 2001, **222**, 427–437.
3 C. T. Campbell, *Science*, 2004, **306**, 234–235.
4 A. S. K. Hashmi and G. J. Hutchings, *Angew. Chem., Int. Ed.*, 2006, **45**, 7896–7936.
5 R. A. Sperling, P. Rivera Gil, F. Zhang, M. Zanella and W. J. Parak, *Chem. Soc. Rev.*, 2008, **37**, 1896–1908.
6 P. K. Jain, K. S. Lee, I. H. El-Sayed and M. A. El-Sayed, *J. Phys. Chem. B*, 2006, **110**, 7238–7248.
7 C. L. Haynes, A. D. McFarland and R. P. Van Duyne, *Anal. Chem.*, 2005, **77**, 338–346.
8 T. S. Ahmadi, Z. L. Wang, T. G. Green, A. Henglein and M. A. El-Sayed, *Science*, 1996, **272**, 1924–1926.
9 G. H. Jeong, M. Kim, Y. W. Lee, W. Choi, W. T. Oh, Q. H. Park and S. W. Han, *J. Am. Chem. Soc.*, 2009, **131**, 1672–1673.
10 I. Ojea-Jimenez, F. M. Romero, N. G. Bastus and V. Puntes, *J. Phys. Chem. C*, 2010, **114**, 1800–1804.
11 M. B. Mohamed, K. M. AbouZeid, V. Abdelsayed, A. A. Aljarash and M. S. El-Shall, *ACS Nano*, 2010, **4**, 2766–2772.
12 M. L. Personick, M. R. Langille, J. Zhang, N. Harris, G. C. Schatz and C. A. Mirkin, *J. Am. Chem. Soc.*, 2011, **133**, 6170–6173.
13 M. H. Huang and P. H. Lin, *Adv. Funct. Mater.*, 2012, **22**, 14–24.
14 Q. Li, B. Lu, L. Zhang and C. Lu, *J. Mater. Chem.*, 2012, **22**, 13564–13570.
15 L. Jiang, Y. Tang, C. Liow, J. Wu, Y. Sun, Y. Jiang, Z. Dong, S. Li, V. P. Dravid and X. Chen, *Small*, 2013, **9**, 705–710.
16 A. S. Barnard, *Acc. Chem. Res.*, 2012, **45**, 1688–1697.
17 T. Ming, W. Feng, Q. Tang, F. Wang, L. D. Sun, J. F. Wang and C. H. Yan, *J. Am. Chem. Soc.*, 2009, **131**, 16350–16351.
18 N. Tian, Z. Y. Zhou, N. F. Yu, L. Y. Wang and S. G. Sun, *J. Am. Chem. Soc.*, 2010, **132**, 7580–7581.
19 Z. Y. Zhou, N. Tian, J. T. Li, I. Broadwell and S. G. Sun, *Chem. Soc. Rev.*, 2011, **40**, 4167–4185.
20 D. Seo, C. I. Yoo, I. S. Chung, S. M. Park, S. Ryu and H. Song, *J. Phys. Chem. C*, 2008, **112**, 2469–2475.
21 L. Zhang, C. Z. Huang, Y. F. Li and Q. Li, *Cryst. Growth Des.*, 2009, **9**, 3211–3217.
22 A. S. Barnard, N. P. Young, A. I. Kirkland, M. A. van Huis and H. Xu, *ACS Nano*, 2009, **3**, 1431–1436.
23 F. Baletto and R. Ferrando, *Rev. Mod. Phys.*, 2005, **77**, 371–423.
24 A. S. Barnard, *Rep. Prog. Phys.*, 2010, **73**, 086502.
25 Y. Wang, S. Teitel and C. Dellago, *J. Chem. Phys.*, 2005, **122**, 214722.
26 H. S. Nam, N. M. Hwang, B. D. Yu and J. K. Yoon, *Phys. Rev. Lett.*, 2002, **89**, 275502.
27 G. Rossi and R. Ferrando, *Nanotechnology*, 2007, **18**, 225706.
28 R. Huang, Y. H. Wen, Z. Z. Zhu and S. G. Sun, *J. Mater. Chem.*, 2011, **21**, 11578–11584.
29 R. Huang, Y. H. Wen, Z. Z. Zhu and S. G. Sun, *J. Mater. Chem.*, 2011, **21**, 18998–19004.
30 Y. H. Wen, R. Huang, C. Li, Z. Z. Zhu and S. G. Sun, *J. Mater. Chem.*, 2012, **22**, 7380–7386.
31 R. Huang, Y. H. Wen, G. F. Shao and S. G. Sun, *J. Phys. Chem. C*, 2013, **117**, 4278–4286.
32 Y. Qi, T. Cagin, W. L. Johnson and W. A. Goddard, *J. Chem. Phys.*, 2001, **115**, 385–394.
33 S. K. R. S. Sankaranarayanan, V. R. Bhethanabotla and B. Joseph, *Phys. Rev. B: Condens. Matter Mater. Phys.*, 2005, **71**, 195415.
34 T. Cagin, Y. Kimura, Y. Qi, H. Li, H. Ikeda, W. L. Johnson and W. A. Goddard, *Mater. Res. Soc. Symp. Proc.*, 1999, **554**, 43–48.
35 A. R. Leach, *Molecular Modelling: Principles and Applications*, Prentice-Hall, London, 2001.
36 D. L. Evans and B. L. Holian, *J. Chem. Phys.*, 1985, **83**, 4069–4074.
37 H. J. C. Berendsen, J. P. M. Postma, W. F. van Gunsteren, A. DiNola and J. R. Haak, *J. Chem. Phys.*, 1984, **81**, 3684–3690.
38 W. C. Swope, H. C. Anderson, P. H. Berens and K. R. Wilson, *J. Chem. Phys.*, 1982, **76**, 637–649.
39 Y. G. Sun and Y. N. Xia, *Science*, 2002, **298**, 2176–2179.
40 Y. N. Wen and H. M. Zhang, *Solid State Commun.*, 2007, **144**, 163–167.
41 Y. Xiang, X. Wu, D. Liu, L. Feng, K. Zhang, W. Chu, W. Zhou and S. Xie, *J. Phys. Chem. C*, 2008, **112**, 3203–3208.
42 J. L. Elechiguerra, J. Reyes-Gasga and M. J. Yacaman, *J. Mater. Chem.*, 2006, **16**, 3906–3919.
43 Y. Xia, Y. Xiong, B. Lim and S. E. Skrabalak, *Angew. Chem., Int. Ed.*, 2009, **48**, 60–103.

 

44 T. Ling, L. Xie, J. Zhu, H. Yu, H. Ye, R. Yu, Z. Cheng, L. Liu, L. Liu, G. Yang, Z. Cheng, Y. Wang and X. Ma, *Nano Lett.*, 2009, **9**, 1572–1576.
45 T. Ling, J. Zhu, H. Yu and L. Xie, *J. Phys. Chem. C*, 2009, **113**, 9450–9453.
46 G. M. Veith, A. R. Lupini, S. Rashkeev, S. J. Pennycook, D. R. Mullins, V. Schwartz, C. A. Bridges and N. J. Dudney, *J. Catal.*, 2009, **262**, 92–101.
47 M. Brust and C. J. Kiely, *Colloids Surf., A*, 2002, **202**, 175–186.
48 C. Kittel, *Introduction to Solid State Physics*, John Wiley & Sons, New York, 1996.
49 S. K. R. S. Sankaranarayanan, V. R. Bhethanabotla and B. Joseph, *J. Phys. Chem. C*, 2007, **111**, 2430–2439.
50 Y. Q. Zhou, M. Karplus, K. D. Ball and R. S. Berry, *J. Chem. Phys.*, 2002, **116**, 2323–2329.
51 H. Lowen, *Phys. Rep.*, 1994, **237**, 249–324.
52 Z. H. Jin, P. Gumbsch, K. Lu and E. Ma, *Phys. Rev. Lett.*, 2001, **87**, 055703.
53 Y. Shibuta and T. Suzuki, *Chem. Phys. Lett.*, 2010, **498**, 323–327.
54 N. Wang, S. I. Rokhlin and D. F. Farson, *Nanotechnology*, 2008, **19**, 415701.
55 J. D. Honeycutt and H. C. Andersen, *J. Phys. Chem.*, 1987, **91**, 4950–4963.
56 Z. L. Wang, Z. Q. Zhong and S. Y. Wang, *Text. Res. J.*, 2012, **82**, 454–462.
57 Y. H. Wen, H. Fang, Z. Z. Zhu and S. G. Sun, *Chem. Phys. Lett.*, 2009, **471**, 295–299.
58 H. L. Anderson, *A Physicist's Desk Reference*, 2nd edn, AIP, New York, 1989.
59 W. H. Li, S. Y. Wu, C. C. Yang, S. K. Lai, K. C. Lee, H. L. Huang and H. D. Yang, *Phys. Rev. Lett.*, 2002, **89**, 135504.